

Radial distribution and strong lensing statistics of satellite galaxies and substructure using high resolution Λ CDM hydrodynamical simulations

Andrea V. Macciò¹ \star , Ben Moore¹, Joachim Stadel¹ & Jürg Diemand^{1,2}

¹*Institute for Theoretical Physics, University of Zürich, Winterthurerstrasse 190, CH-8057 Zürich, Switzerland*

²*Department of Astronomy & Astrophysics, University of California, 1150 High Street, Santa Cruz CA 95064, USA*

6 March 2018

ABSTRACT

We analyse the number density and radial distribution of substructures and satellite galaxies using cosmological simulations that follow the gas dynamics of a baryonic component, including shock heating, radiative cooling and star formation within the hierarchical concordance Λ CDM model. We find that the dissipation of the baryons greatly enhances the survival of subhaloes, especially in the galaxy core, resulting in a radial distribution of satellite galaxies that closely follows the overall mass distribution in the inner part of the halo. Hydrodynamical simulations are necessary to resolve the adiabatic contraction and dense cores of galaxies, resulting in a total number of satellites a factor of two larger than found in pure dark matter simulation, in good agreement with the observed spatial distribution of satellite galaxies within galaxies and clusters. Convergence tests show that the cored distribution found by previous authors in pure N-body simulations was due to physical overmerging of dark matter only structures.

We proceed to use a ray-shooting technique in order to study the impact of these additional substructures on the number of violations of the cusp caustic magnification relation. We develop a new approach to try to disentangle the effect of substructures from the intrinsic discreteness of N-Body simulations. Even with the increased number of substructures in the centres of galaxies, we are not able to reproduce the observed high numbers of discrepancies observed in the flux ratios of multiply lensed quasars.

Key words: cosmology: theory – dark matter – large-scale structure of the Universe – galaxies: clusters – galaxies: haloes – methods: numerical

1 INTRODUCTION

The study of substructures within simulated galaxy sized haloes have posed interesting problems to the current, widely accepted, Λ CDM scenario. As pointed out previously, (Klypin et al 1999, Moore et al. 1999) the number of surviving subhaloes found in N-Body simulations greatly exceeds the number of observed satellites around the Milky Way and Andromeda. The properties of subhaloes on different scales has been the subject of many recent studies which have pushed the resolution of dissipationless simulations (Moore et al. 1998, Ghigna et al. 1998, Colin et al. 2000, Ghigna et al 2000, Springel et al. 2001, De Lucia et al. 2004, Kravtsov et al 2004, Diemand et al 2004a, Gao et al 2004a, Reed et al 2005, Zentner et al 2005a, Zentner et

al 2005b). The kinematical properties of subhaloes are now well understood - they make up a fraction of between 5 and 10% of the mass of virialized haloes on scales relevant to observational cosmology.

Most of these previous studies used dissipationless cosmological simulations; although non-baryonic dark matter exceeds baryonic matter by a factor of $\Omega_{dm}/\Omega_b \simeq 6$ on average, the gravitational field in the central region of galaxies is dominated by stars and gas. In the hierarchical galaxy formation model, stars are formed by the condensation of cooling baryons at the halo center. The cooling baryons increase the density in the central halo region mainly because of the extra mass associated with the inflow, but also because of the adiabatic contraction of the total mass distribution (Blumenthal et al (1986), Loeb & Peebles (2003), Gao et al. (2004b), Gnedin et al. (2004)). This process acts *both* for the host halo and its subhaloes, therefore we may ex-

\star andrea@physik.unizh.ch

pect that the dark matter substructure haloes formed within hydrodynamical simulations will experience a different tidal force field and they themselves will be more robust to tidal effects. Since overmerging of dark matter substructures is sensitive to their central structure (Moore, Katz & Lake 1996), pure N-Body simulations may bias results because of physical overmerging (Diemand, Moore & Stadel 2004a, DMS04 hereafter).

The fact that substructure haloes are spatially more extended than the averaged mass distribution was first pointed out by Ghigna et al. (1998). By increasing the resolution by over an order of magnitude, DMS04 showed that this result was independent of the numerical resolution. Furthermore the distribution of galaxies in clusters appears to follow the overall mass distribution, quite unlike the subhaloes selected by final bound mass in pure dark matter simulations. By tracing haloes backwards and forwards in time through the simulations they argued that the missing central subhaloes may be destroyed by tidal forces at redshifts higher than $z=5$. The survival of substructure and galaxies within dense environments has implications for indirect detection techniques, for example using image distortions of gravitationally lensed distant quasars by foreground galaxies and their dark matter haloes.

It has been argued that a possible signature of the presence of dark matter substructures can be found in strong gravitational lensing of QSOs (Mao & Schneider 1998; Metcalf & Madau 2001; Chiba 2002; Metcalf & Zhao 2002; Dalal & Kochanek 2004; Chen, Kravtsov & Keeton 2003; Kochanek & Dalal 2004; Mao et al 2004, Amara 2004). If a distant image source is close to (or inside) a cusp in a caustic curve, three of the images will be clustered together and the sum of their magnifications will be zero (Zakharov (1995), taking the negative parity image to have negative magnification). This relation holds for a wide class of smooth analytic lens models (i.e. Schneider & Weiss 1992, Keeton et al. 2003); on the other hand all known observed lensed QSOs violate this relation which has been explained as due to the presence of cold dark matter substructure within the lensing galaxy's halo. However, some of these discrepant systems may be due to microlensed stars rather than to cold dark matter substructure (Keeton et al 2003). Bradac et al. (2004) analysed a low resolution simulation of a galaxy and claim that the level of substructure present in simulations produces violations of the cusp relation comparable to those observed. Amara et al. (2004) implanted an idealised model of galaxy into the center of a high resolution galactic halo extracted from dissipationless N-Body simulations to test the effects of substructure on lensed images. Their findings contrast those of Bradac et al 2004, since they found that the substructures produced in a Λ CDM halo are not abundant enough to account for the cusp caustic violation observed, these results are also confirmed by Mao et al 2004, based on analysis of substructure abundance in pure dark matter simulations.

The first part of this paper is devoted to the analysis of the subhalo population around a galaxy sized halo that forms in a large cosmological simulation simulated with dark matter only and then with the inclusion of a baryonic component. In section 2 we present the numerical simulations, our halo-finding scheme and resolution tests. The properties of the main halo and its satellites are presented in sec-

tion 3. Comparison with observations and a discussion of the results are in section 4. In the second part of this paper we re-examine the effects of substructures on multiply lensed quasar images using our new hydrodynamic galaxy simulation in combination with a ray shooting technique. In section 5.1 we present the lensing code, while section 5.2 is devoted to multiple images analysis and in sections 6 and 7 we present our results and the conclusions of our work.

2 NUMERICAL SIMULATIONS

The simulations were performed with GASOLINE, a multi-stepping, parallel TreeSPH N -body code (Stadel 2001, Wadley et al. 2004). We include radiative and Compton cooling for a primordial mixture of hydrogen and helium. The star formation algorithm is based on a Jeans instability criteria (Katz 1992), where gas particles in dense, unstable regions and in convergent flows spawn star particles at a rate proportional to the local dynamical time (see also Governato et al 2004). The star formation efficiency was set to 0.1, but in the adopted scheme its precise value has only a minor effect on the star formation rate (Katz 1992). The code also includes supernova feedback as described by (Katz 1992), and a UV background following Haardt & Madau 1996.

We have selected a candidate Galactic mass halo ($M_{dm} \approx 10^{12} M_{\odot}$) from an existing low resolution dark matter only simulation in a concordance ($\Lambda=0.7, \Omega_0=0.3, \sigma_8=0.9$) cosmology and resimulated it at higher resolution using the volume renormalization technique (Katz & White 1993), and including a gaseous component within the entire high resolution region. The mass per particle of the dark matter and gaseous particles are respectively $m_d = 1.66 \times 10^6 M_{\odot}$ and $m_g = 3.28 \times 10^5 M_{\odot}$. The dark matter has a spline gravitational softening length of 200 pc and we have about 1×10^6 particles for each component (dark and gas) in the high resolution region.

The SPH simulations with cooling are computationally expensive and we are forced to stop the full calculation once the galaxy has formed, at a redshift $z = 1.5$. (The parallel calculation is dominated by the few remaining gas particles which need extremely small timesteps in order to satisfy the Courant criterion). In order to study the dynamical evolution of the stellar and dark matter satellites we have evolved the simulation to the present epoch without following the remaining gaseous particles - we turn them into collisionless particles and treat only their gravitational interactions. We do not believe that this influences any of our conclusions since (i) most of the gas has already turned into stars between a redshift $z=5.5$ and $z=2.5$, and (ii) continuing to include cooling of the remaining gas would only allow us to resolve higher density gas clouds. Inside the virial radius at a redshift $z=0$ we have 8.6×10^5 dark matter particles and 2.4×10^5 star particles. In Figure 1 we show the star formation rate in our simulation which is in good agreement with previous numerical studies (i.e. Governato et al. 2004).

The same object has also been simulated with dark matter only using the same spatial and mass resolution as the hydro run, in addition one simulation with four times better mass resolution (this object is Gal1 in DMS04). In the following we will refer to the three simulations as *hydro*, *dm* and *dm_{HR}* respectively.

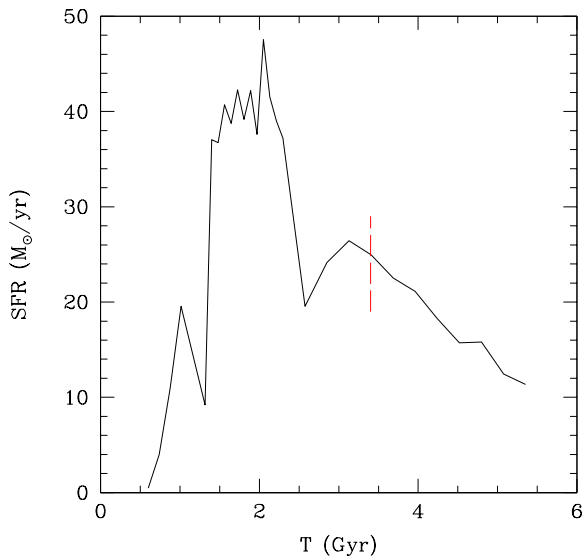


Figure 1. The star formation rate in the hydro simulation. The time since the big-bang is indicated and the red vertical line corresponds to $z = 2$, where cooling were switched off.

3 HALOES PROPERTIES

3.1 Host halo

In Figure 2 we show the rotation curve (defined as $V_c(r) = \sqrt{GM(<r)/r}$) for all components, stars and dark matter separately for the galaxy at $z=0$. For comparison we also show the dark matter rotation curve obtained in the pure dark matter simulation of the same object. The baryons dominate within the inner 10 kpc and the effect of the adiabatic contraction on the dark matter can be clearly seen - the baryons have increased the mass within 5 kpc by a factor of four. The steeper central cusp can be clearly seen in the density profile plot (fig. 3), the dm halo has a profile that can be well fitted by an NFW profile with a concentration $c_{vir} = 9.6$ (defined with respect to the virial radius); on the other hand in the presence of gas and stars the density profile in the inner region has an almost constant cusp slope $\alpha \approx -2.0$, as predicted by the adiabatic contraction model (Blumenthal et al. 1986). In figure 1 we show the star formation rate (SFR), the bulge of the galaxy forms through a series of rapid major merger events that end around $z = 2.8$, turning mostly low angular momentum gas into stars. There are no more merging events in the formation of our galaxy after $z = 2$ so even if we cannot follow the SFR directly beyond $z = 1.5$ we do not expect it to be different from a slowly decreasing function of time.

3.2 Sub haloes

Within the virial radius of the high resolution CDM simulations we can resolve several hundreds of substructure haloes (bound over-dense clusters of particles). We identify subhaloes with SKID (Stadel 2001), which calculates local densities using an SPH kernel, then moves particles along the density gradient until they oscillate around a point (i.e. move

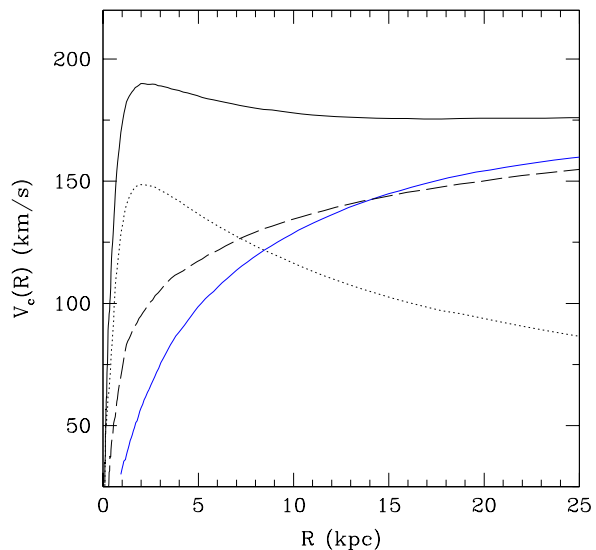


Figure 2. Rotation curve (defined as $V_c(R) = \sqrt{GM(<R)/R}$) for all components (upper solid line), star (dotted line) and dark matter (dashed line) for the galaxy at $z=0$. For comparison the dark matter rotation curve (lower solid line) obtained in the pure dark matter simulation of the same object is also shown.

less than some length l). Then they are linked together using FoF with this l as a linking length.

SKID with $l = 4\epsilon_0$ (where ϵ_0 is the gravitational softening of the simulation) adequately identifies the smallest subhaloes and the centers of the largest subhaloes. For the latter the calculated bound mass is underestimated. Using $l = 10\epsilon_0$ can cure this, but then some of the small subhaloes are missed. Therefore we have used a combination of the subhalo catalogues obtained with these two linking lengths in order to create the complete catalogue of subhaloes and to calculate their correct structural parameters. We included in our study only halos with $M > 2 \times 10^8 M_\odot$ (i.e. $n_{dm} > 100$).

In Figure 4, where we plot the dark matter subhaloes mass function in the *hydro* and *dm* simulations, calculated within a sphere of radius 1 Mpc centred on the galaxy. As expected, we do not observed a big difference between the two simulations in such a large volume, this is because the presence of baryons is thought to be much more important in the inner region of our galaxy where the tidal field is much more efficient in destroying subhaloes. The effect of baryons can be easily seen in Figure 5, where we plot the ratio of the number of subhaloes in the two simulations as function of the distance from the center of the galaxy. At 70 kpc ($\approx 1/3R_{200}$) we see an increase by a factor of two in the numbers of surviving satellites. Within the inner 40 kpc the number of satellites with mass greater than $2 \times 10^8 M_\odot$ is enhanced by a factor 4-5 over that found in the pure dark matter simulation. We found that this difference is more striking for the most massive subhaloes, the number of satellites with mass greater than $10^7 M_\odot$ does not differ so much from the N-body result. This may be revealing the limitation of our resolution - the smallest haloes of mass $\sim 10^7 M_\odot$ are just resolved with about 10 DM particles and are more easily

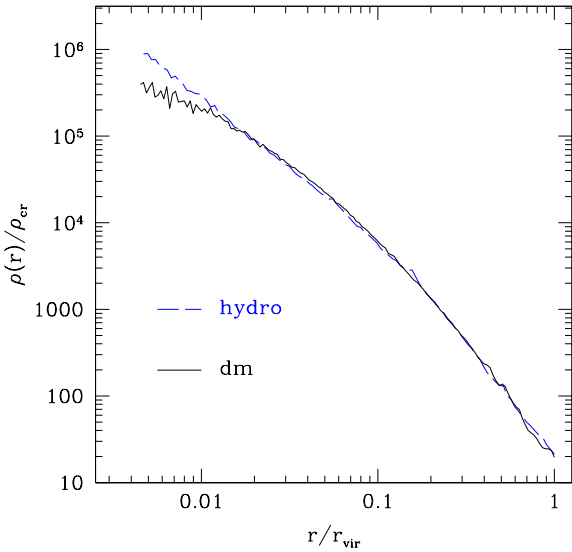


Figure 3. Dark matter density profile in the N-Body (dashed curve) and Hydro (solid line) simulations, the effect of the adiabatic contraction can be clearly seen in the inner part of the profile.

destroyed through numerical effects. Another explanation could be the inhibition of star formation in smaller haloes because of the ultra-violet (UV) background and supernovae (SN) feedback that raise the temperature of the gas and stop its collapse in the DM halo if it is not sufficiently bound (i.e. its potential well is not deep enough). Without stars, the DM can be more easily destroyed by the tidal forces of the main halo (see also section 4 for more details on the feedback effects).

As noticed by previous authors (DMS04 for a recent analysis) the spatial distribution of subhaloes in cold dark matter simulations of galaxies is anti-biased with respect to the mass; Nagai & Kravtsov (2005) have recently shown that part of this bias is due to the varying amount of mass loss at different radii, and that it is considerably smaller if instead of using the mass of satellites at $z = 0$, one uses the mass measured at the accretion time. For our purposes we have decided to use the mass at the present time, because we are interested in the different tidal forces and mass loss between the *hydro* and *dm* run.

Figure 6 shows the relative number density of surviving satellites $M > 2 \times 10^8$ at $z=0$, in several pure dark matter simulations and our hydro simulation. In all *dm* cases, the satellites are more extended than the overall mass distribution (dominated by the smooth dark matter background). This effect becomes larger inside of half the virial radius. Within this region, the dark matter only simulations reveal a much flatter number density distribution. The satellite distribution in the hydro simulation is much steeper and it is rather similar to the smooth mass distribution even if also in this case the overall radial distribution of the subhalos is more extended than the underlying dark matter distribution as shown clearly by the excess in the number density of subhalos at $0.5 < r/r_{vir} < 1.0$.

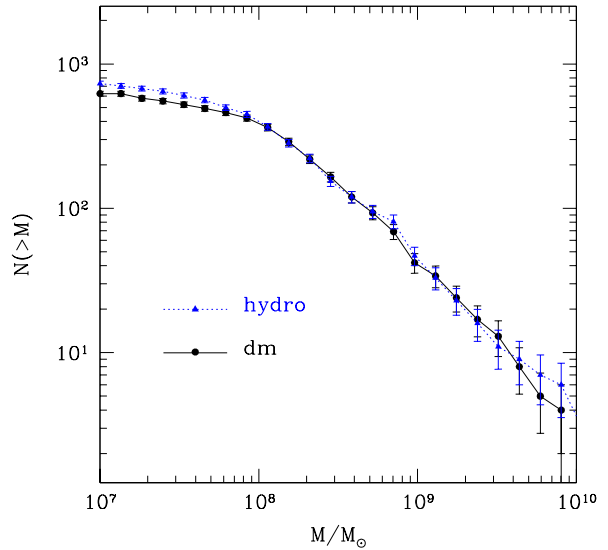


Figure 4. Dark matter subhaloes mass function in the *hydro* (black) and *dm* (blue) simulations, in a sphere of 1 Mpc around the center of the galaxy.

The inner core distribution found in the *dm* run almost disappears and the satellite profiles are well fitted by an NFW like function even if they are still less concentrated than the overall mass distribution (in agreement with findings from hydro simulations on cluster scales by Nagai & Kravtsov (2005)); the concentration parameter (r_{vir}/r_c) for the satellite distribution is ≈ 6.5 , where the one for the smooth DM distribution in the range $0.07 < r/r_{vir} < 1.0$ is $c_{DM} = 9.6$.

3.3 Resolution tests

In the hydro simulation we have a higher mass resolution due to the presence of baryons; the mass of the star and gas particles is roughly 20% of the mass of the DM particles, this means that in principle the lower number of subhaloes close to the center that we found in the N-Body simulation can be partially due to an overmerging phenomenon that depends on the resolution. In the lower panel of Figure 7 we compare the number of subhaloes as a function of radius between the hydro simulation and the highest resolution dark matter only run (*dm_{HR}*) which has a mass resolution a factor 4 better than the low resolution case. Figure 7 demonstrates that the increase in the number of substructure haloes in the hydro run is apparent even when compared to the higher resolution N-Body simulation.

The second test that we have performed is related to the force resolution (gravitational softening) adopted for the star particles. Stars are concentrated in the inner few kpc of the galaxy and a small softening must be chosen to correctly follow the dynamical evolution of such high density regions. We have run the hydro simulation for two different values of the star gravitational softening (ϵ): $\epsilon_1 = 0.2$ kpc and $\epsilon_2 = 1.5$ kpc. Results are presented in the upper panel of Figure 7 where we show the difference in the number of

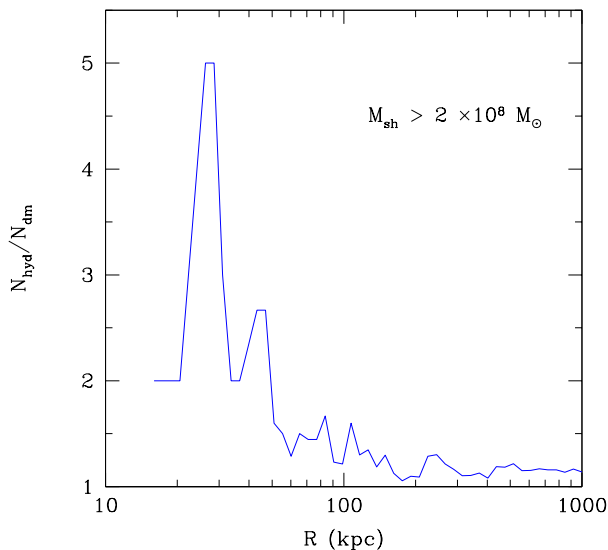


Figure 5. Ratio between the number of DM subhaloes with $M > 2 \times 10^8 M_{\odot}$ in the *hydro* and *dm* runs as function of the distance from the center of the main halo.

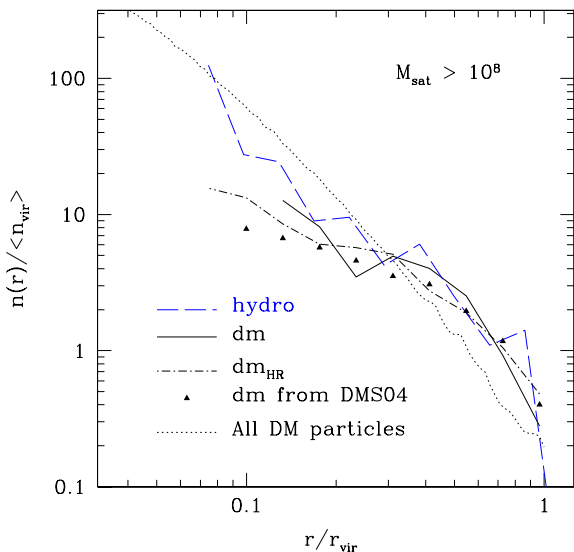


Figure 6. Substructure radial density profiles for different simulations.

subhaloes as a function of the distance from the center. The effect of softening is important - too large a value leads to tidal disruption of satellite galaxies since they have artificially shallow central potentials and are hence less bound. The larger stellar softening ($\epsilon_2 = 1.5$ kpc) erases the stabilizing effect of the stars inside the satellites and the radial distribution of surviving subhaloes is identical to the pure dark matter case (see the dashed line in the upper panel of Figure 7).

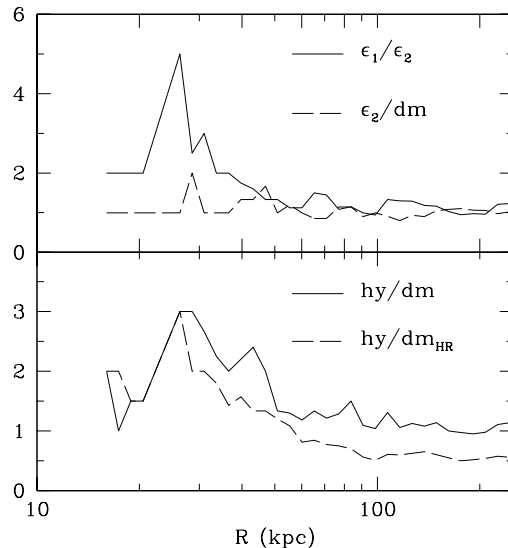


Figure 7. Effect of resolution on the number of subhaloes. *Upper panel:* ratio between the number of DM subhaloes ($M > 2 \times 10^8 M_{\odot}$) in the *hydro* run for two different values of the star particles softening: $\epsilon_1 = 0.2$ kpc and $\epsilon_2 = 1.5$ kpc as function of distance from the center. The dashed line is the same quantity but for the *hydro* run with $\epsilon = \epsilon_2$ and the *dm* run. *Lower Panel:* the ratio between the number of DM subhaloes ($M > 10^7 M_{\odot}$) in the *hydro* run and in the high resolution *dm_{HR}* (dashed line) and low resolution *dm* (solid line) runs.

4 COMPARISON WITH OBSERVATIONS

For this comparison we used the data for the Local Group as compiled by Mateo et al. (1998). In this sample only relatively massive satellites with an estimated rotational velocity or a three-dimensional velocity dispersion of stars greater than 10 km sec^{-1} are considered. In order to simplify the comparison even further, as Klypin et al. (1999) we have considered the number of satellites within a radius of 280 kpc from the Milky Way and Andromeda, which is close to the expected virial radius of these galaxies.

Even though the remaining gas particles are turned into collisionless tracers at $z = 1.5$, this does not affect the kinematical properties of the satellites at $z=0$. All of the satellites that end up within the virial radius of the galaxy halo have formed prior to this epoch. Subsequent loss of the remaining gas particles to stars or by stripping processes would not lead to significant changes to the satellite structural parameters.

In Figure 8 we show the cumulative velocity distribution function (VDF) of satellites: the number of satellites per unit volume and per central object with internal circular velocity larger than a given value V_c . We show the VDF for different runs: the solid line represents the results for the *dm* simulation, as already known the CDM models over-predict the number of satellites for $V_c < 30 \text{ km sec}^{-1}$. The dashed line represent the results from Klypin et al 1999, that were originally compared with the data from Mateo et al 1998. The simulation results agree quite well above 20 km sec^{-1} , our higher resolution pure dark matter simulations allow

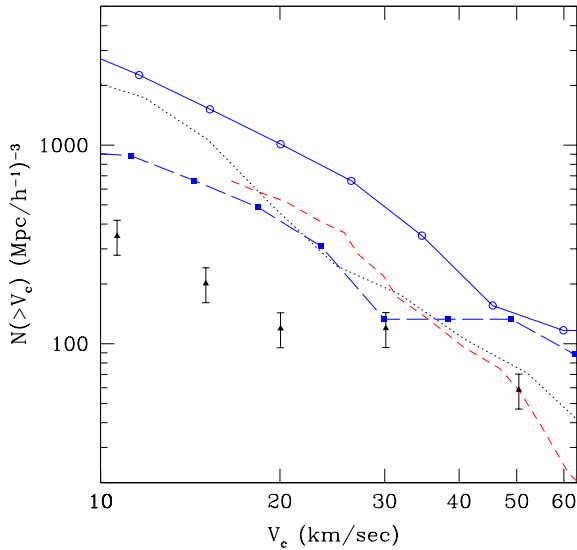


Figure 8. Cumulative circular velocity distribution function of satellites. Black solid line represents the results for the DM only simulation, blue solid line is the VDF for stars (visible) haloes, the dashed blue line is for DM haloes. Black triangles with error bars show average results for Milky Way and Andromeda Satellites (Mateo 1998 & Klypin et al 1999). The red dashed line are results for a Λ CDM dissipationless galaxy obtained by Klypin et al (1999).

us to follow the distribution of subhaloes to lower circular velocities ($V_c > 10 \text{ km sec}^{-1}$).

The open circles connected by a solid line shows the VDF of dark matter haloes for the hydro run. The numbers of satellites in the range $15 < V_c < 30 \text{ km sec}^{-1}$ is increased, and now also for $V_c > 35 \text{ km sec}^{-1}$ there is an over abundance of satellites. We have also computed the VDF for satellites in the hydro run considering only their stars, shown by squares connected with the long dashed line. This is a fairer comparison since we are comparing stellar kinematics in each case. Stars are more concentrated than DM, so they trace the dynamics within a smaller central region, this explains why the VDF for stars is below the DM one over the whole velocity range (Hayashi et al 2004) but this effect is much too small to reconcile the simulations with the observations of Local Group satellites.

Another clear difference between the two VDFs is that we have no stellar satellites with $V_c < 15 \text{ km sec}^{-1}$, which is due to the supernovae feedback and UV background in the simulation. To confirm this we have run a full hydrodynamical simulation without these external feedback sources, shown in fig. 9, where the VDF for the no feedback case continues to rise within $V_c < 15$. With the weak feedback used in this paper hydrodynamic cosmological simulations produce VDFs which lie above the pure dark matter results and the discrepancy to Local Group observations becomes even larger. Runs with strong feedback from reionization are able to produce realistic VDFs, we will present such runs in a forthcoming paper (Macciò et al. 2005b).

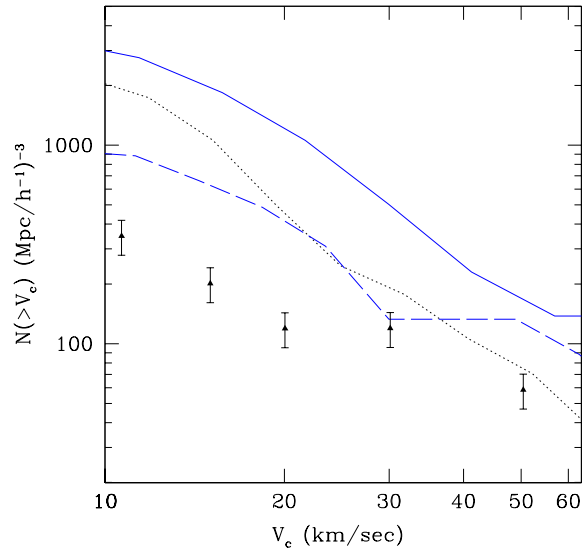


Figure 9. A similar plot to figure 8: the solid (blue) line is the stellar satellite VDF in absence of SN feed back, the dashed line is with feedback turned on, black dotted line represents the results for the DM only simulation.

5 LENSING ANALYSIS

Quasars that are being gravitationally lensed into multiple images have recently been used to place limits on the surface density of cold dark matter subhaloes (Mao & Schneider 1998, Metcalf & Madau 2001, Chiba 2002, Metcalf & Zhao 2002, Dalal & Kochanek 2002, Chen Kravtsov & Keeton 2003, Bradac et al. 2004, Mao et al 2004, Amara et al. 2004). Small mass clumps that happen to lie near the images affect the observed magnification ratios. The question arises as to whether these observations are compatible with distortions expected to occur from dark matter substructures and satellite galaxies within the Λ CDM model. In the following we will first present our lensing code, then we will briefly recall the main features of the so called “Cusp Relation” and finally we will report our results.

5.1 Lensing Simulations

Our ray shooting code is described in detail in Macciò 2005, here we will only summarize its main features. The galaxy is centered in a cube of length 0.6 Mpc and we study three lense images, obtained by projecting the particle positions along the three coordinate axes. We then divide the projected density field Σ by the critical surface mass density for lensing

$$\Sigma_{cr} = \frac{c^2}{4\pi G} \frac{D_S}{D_L D_{LS}}, \quad (1)$$

thus obtaining the convergence k . Here c is the speed of light, G is the gravitational constant, while D_L , D_S , D_{LS} are the angular-diameter distances between lens and observer, source and observer, lens and source, respectively. In the following, we adopt $z_L = 0.3$ for the lens redshift and $z_s = 3.0$ for the source redshift.

The deflection angle due to this 2D particle distribution, on a given point \vec{x} on the lens plane reads:

$$\vec{\alpha}(\vec{x}) = \sum_{j=1}^N \frac{4G}{c^2} \frac{m_j}{|\vec{x} - \vec{y}_j|}. \quad (2)$$

Here \vec{y}_j is the position of the j -th particles and N is the total number of particles.

Since a direct summation requires a long time, we speed up the code by using a P³M-like algorithm: the lens plane was divided into 256×256 cells and direct summation was applied to particles belonging to the same cell of \vec{x} and for its 8 neighbor cells. Particles in other cells were then seen as a single particle in the cell baricenter, given the total mass of the particles inside the cell. The deflection angle diverges when the distance between a light ray and a particle is zero. To avoid this unwanted feature we introduce a softening parameter, ϵ in equation (2); the value ϵ is tuned to the resolution of the current simulation.

We start to compute $\vec{\alpha}(\vec{x})$ on a regular grid of 4096×4096 test rays that cover the central quarter of the lens plane (multiple images form very close to the lens center). This resolution does not provide enough pixels in the inner regions affected by strong lensing to model lensing properties in the correct way. The resolution is increased by extracting the central region where strong lensing is occurring and using bilinear interpolation to calculate the relevant quantities to higher resolution. Our final resolution is equivalent to a bundle of 16384×16384 light rays.

The relation between image and sources positions is given by the lens equation:

$$\vec{y} = \vec{x} - \vec{\alpha}(\vec{x}) \quad (3)$$

and the local properties of the lens mapping are then described by the Jacobian matrix of the lens equation,

$$A_{hk}(\vec{x}) = \frac{\partial y_h}{\partial x_k} = \delta_{hk} - \frac{\partial \alpha_h}{\partial x_k} \quad (4)$$

and the magnifications factor μ is given by the Jacobian determinant of A ,

$$\mu(\vec{x}) = \frac{1}{\det A} = [A_{11}(\vec{x})A_{22}(\vec{x}) - A_{12}(\vec{x})A_{21}(\vec{x})]^{-1}. \quad (5)$$

Finally, the Jacobian also determines the location of the critical curves \vec{x}_c on the lens plane, which are defined by $\det A(\vec{x}_c) = 0$. Because of the finite grid resolution, we can only approximately locate them by looking for pairs of adjacent cells with opposite signs of $\det A$. Then the lens equations

$$\vec{y}_c = \vec{x}_c - \vec{\alpha}(\vec{x}_c), \quad (6)$$

yields the corresponding caustics \vec{y}_c , on the source plane.

To find the images of an extended source, all image-plane positions \vec{x} are checked to see if the corresponding entry in the map table \vec{y} lies within the source: i.e. for a circular source with radius r_c and centered in $(y_1^c; y_2^c)$ it is checked if:

$$(y_1 - y_1^c)^2 + (y_2 - y_2^c)^2 \leq r_c^2, \quad (7)$$

where (y_1, y_2) are the components of the vector \vec{y} . The sources are modeled as circles with a radius of 60 pc according to Amara et al (2004). Those points fulfilling the previous equation are part of one of the source images and

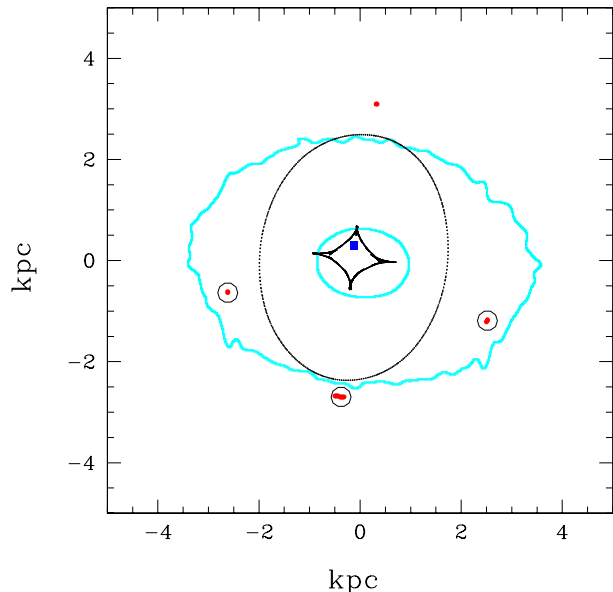


Figure 10. Basic lens configuration. The caustic surface is shown as a black line and critical curves are shown as cyan lines. The four images that are usually observed are shown as red dots, and the three that are used to inspect the cusp relations are the ones inside the small black circles. The blue square is the source position. The softening adopted for this lens map is 0.5 Kpc.

are called image points. We then use a standard *friends-of-friends* algorithm to group together image points within connected regions, since they belong to the same image.

A typical lens configuration is shown in Figure 10 where critical lines, caustic lines, source and images position are indicated. The images within the black circles correspond to the those selected for the cusp relation investigation.

5.2 Cusp Caustic Relation

There are basically three configurations of four-image systems: fold, cusp, and cross. In this paper we will mainly concentrate on the *cusp* configuration, that corresponds to a source located close to the cusp of the inner caustic curve. The behavior of gravitational lens mapping near a cusp was first studied by Blandford & Narayan (1986), Schneider & Weiss (1992) and Mao (1992) and Zakharov (1995), who investigated the magnification properties of the cusp images and concluded that the sum of the signed magnification factors of the three merging images approaches zero as the source moves towards the cusp. In other words (e.g. Zakharov 1995) :

$$R_{cusp} = \frac{\mu_A + \mu_B + \mu_C}{|\mu_A| + |\mu_B| + |\mu_C|} \rightarrow 0, \quad \text{for } \mu_{tot} \rightarrow \infty \quad (8)$$

where μ_{tot} is the unsigned sum of magnifications of all four images, and A, B & C are the triplet of images forming the smallest opening angle. By opening angle, we mean the angle measured from the galaxy center and being spanned by two images of equal parity. The third images lies inside such an angle. This relation is an asymptotic relation and holds

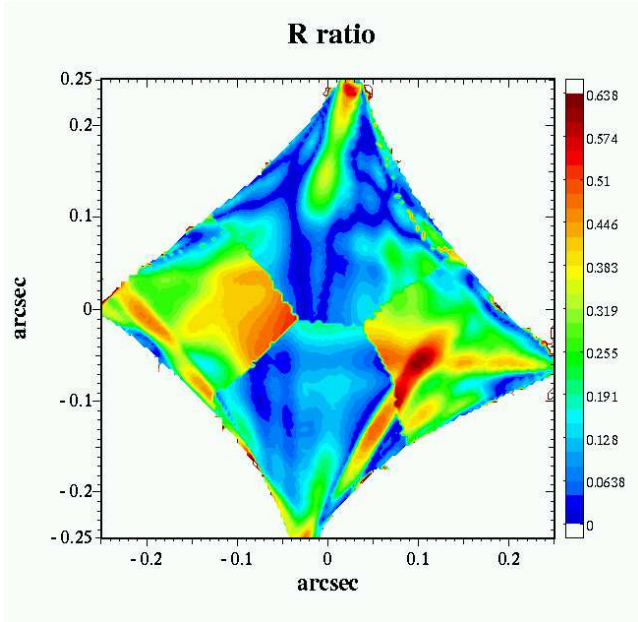


Figure 11. Value of the quantity R_{cusp} in the four images region of the source plane, here a softening of 0.3 Kpc is used.

when the source approaches the cusp from inside the inner astroid caustic.

Since we know the lens position and the source position the procedure of finding the cusp images is straightforward, we have identified the triplet of images belonging to the smallest opening angle, we have seen that the cusp images are better identified using as opening angle measured from the fourth image and being spanned by two images of equal parity. We have used this method only to find the cusp images, instead for testing the cusp relation (see eq. 9) we have used the opening angle as defined from the center of the galaxy ($\Delta\theta$).

Approximately 25000 lens systems are generated with the source position inside the astroid caustic. Figure 11 indicates in color the value of R_{cusp} for all the different source positions; the apparent discontinuities originate from different image identifications. In the very center of the caustic the cusp relation is not well defined (what you have is mostly a “cross relation”, four images situated at the vertices of a cross centered on the cusp center), as the source moves in the direction of the minor or major axes we choose different subsets of three cusp images and therefore the discontinuity arises.

6 EFFECTS OF SUBSTRUCTURES

Because of the finite size (discreteness) of the particles in the simulations there is a significant amount of shot noise in the surface density estimate, which can affect the lensing properties. The usual approach (Bradac et al. 2004, Amara et al. 2004) is to use a Gaussian kernel to smooth the surface density, in Amara et al. (2004) a detailed study of the impact and calibration of the smoothing was presented, their main conclusion was that a smoothing of 0.5 kpc is suitable for studying the cusp relation properties without losing any spatial information.

In order to try to disentangle the effects of bound substructures to the spurious effect produced by single finite particles, we have adopted a novel approach. We have tried to *remove* substructures from the lensing halo to see how this can change the cusp relation. Our removal procedure works as follows: first we identified all bound substructure using SKID (see section 3.2), then each particle belonging to any of the subhaloes is rotated around the center of the galaxy using three random Euler angles. In order to avoid thin circular shells of particles we added a random $\pm 10\%$ error to each distance. We want to emphasize that we do not physically remove any substructures, because this will change the overall properties of the lens: mass, density profile, etc.

This procedure allows us to smooth out only the substructures leaving unaltered all the main features of the primary lens. In Figure 14 (upper panel) we show the integral radial mass profile before and after the *removal* of the substructures, not only the total mass is preserved but also its radial profile, this means that all the lensing properties of the galaxy remain unchanged (critical curves, caustics, position of images) allowing us to make a one to one comparison between the two lensing maps. In Figure 12 and Figure 13 the density map of the galaxy is shown, with and without substructures respectively.

The cusp relation defined by equation 8 holds when the source is close to the cusp. As soon as the source moves away from the cusp deviations from $R_{cusp} = 0$ are observed, even for the smooth lens model. On the other hand the closer the source is to the cusp, the smaller is the angle spanned from the three images, so in order to take into account also the position of the source in evaluating the cusp relation it is better to define R_{cusp}^0 as (see also Amara et al. 2004):

$$R_{cusp}^0 = \frac{2\pi}{\Delta\theta} R_{cusp}. \quad (9)$$

where $\Delta\theta$ is the opening angle spanned by the two images with positive parity defined from the center of the galaxy.

With this new definition of R_{cusp}^0 a set of three images is said to violate the cusp relation if $R_{cusp}^0 > 1$. This makes the comparison between simulations and observations much more straightforward.

The differences in the reduced cusp relation violation in the two cases are shown in Figure 16, where we plot the number of sources that violate the *reduced* cusp relation as a function of the Gaussian smoothing scale (ϵ_g). For both the lens models, the number of sources that violate equation 9 decreases with the smoothing length because the effect of smoothing is to both reduce the impact of substructures and the noise introduced by single particles.

The difference between the two is not so large, with a maximum for $\epsilon_G = 0.5$ kpc, where the number of violations grows from 19% to 23%, this is because this value of ϵ_G is large enough to cancel the Shot noise, but not large enough to smear out the subhaloes in the simulation, in good agreement with the results of Amara et al. For smaller value of ϵ_G the signal is almost completely dominated by Shot noise, and for larger values we smooth too much, losing spatial information on the surface density of the lens.

Figure 16 clearly shows that the impact of substructure in a mass range $10^7 - 10^9$ is very weak in disturbing the cusp relation. The resolution achievable with current

numerical simulations is still too poor to extend the analysis to a lower mass range of subhaloes, analytic arguments or semi-analytic prescriptions must be used (Macciò & Miranda 2005).

Nevertheless a tentative comparison with observation can be made; there are 5 observed cusp caustic lenses systems: B0712+472 (Jackson et al 1998), B2045+265 (Koopmans et al 2003), B1422+231 (Patnik & Narasimha 2001), RXJ1131-1231 (Sluse et al. 2003) and RXJ0911+0551 (Keeton et al 2003); the first three are observed in the radio band, the last two in optical and IR. Three of them violate the reduced cusp relation (i.e. $R_{cusp} > \Delta\theta/2\pi$). This means a 60% violation, that is significantly larger than the 15-25% we found for our simulations. The sources size used in this work (60pc) allows us to make a direct comparison mainly with QSO observed in radio than in optical or IR, even in this case we have a violation of the reduced cusp relation in 2 objects over 3, that means 66% violation. Figure 15 shows the distribution of the values of the reduce cusp relation R_{cusp}^0 both for data and simulates systems (with $\epsilon_G = 0.5$ kpc). Simulation results are unable to reproduce the high value tail that arises in the observational data; again it is possible to see that the effect of subhaloes is very weak in disturbing the cusp relation, and they only marginally enhance the number of systems with $R_{cusp}^0 > 1$.

As already discussed above, the difference between data and simulation results can arise from the current resolution limitations in the Numerical simulations, we expect to have many more small DM haloes close to the center of the galaxy with masses in the range $10^{-3} - 10^6 M_\odot$, these haloes will be very concentrated and so they can more easily survive the tidal force of the central halo and if one of these haloes is close enough to one of the images it can perturb its magnification and so violate the cusp relation. (the smaller is the mass of the subhalo the closer it must be to the projected image position).

Another possible explanation for the observed cusp relation violation, can be ascribed to the effect of the all subhaloes that are in the galactic space along the line of sight of the lens (Metcalf 2004); the importance of these intergalactic haloes with mass $< 10^8 M_\odot$ depends on the radial profile of the dark matter haloes and the primordial power spectrum at small scales.

What is clear from our analysis is that the cusp relation violation can not be due to substructures in the primary lens with a masses above $10^7 M_\odot$. This is true even though the inclusion of baryons has increased the projected numbers of subhaloes by a large factor.

7 DISCUSSION AND CONCLUSIONS

Using a high resolution hydrodynamic galaxy formation simulation we have studied the number density and the spatial distribution of subhaloes within a Milky Way sized CDM halo. Baryons can concentrate at the halo centre via two mechanisms: The shock heated gas can radiate away energy causing the particles to fall inwards. Cold gas clouds can accrete along filaments, colliding and coalescing with existing gas at the halo centre. The slowly infalling baryons has the effect of increasing the density of the dark matter via adiabatic contraction. The overall effect of including

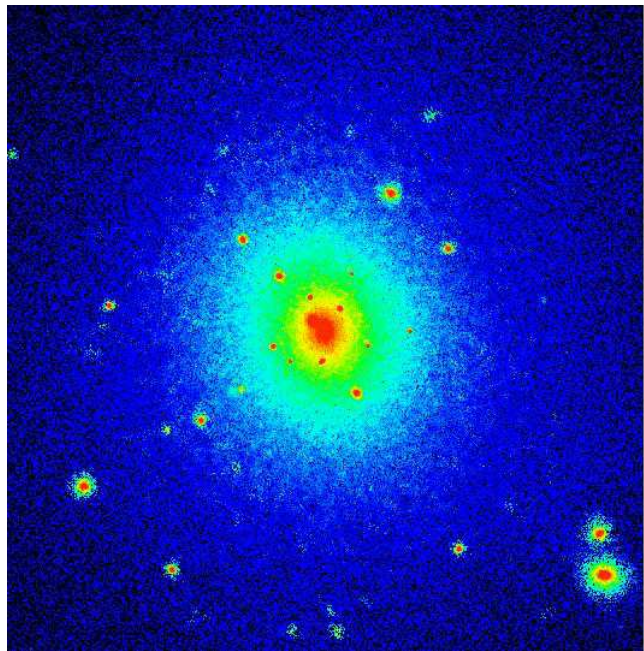


Figure 12. Density map of the mass distribution within the full hydrodynamical simulation. The size of the box is 200 kpc.

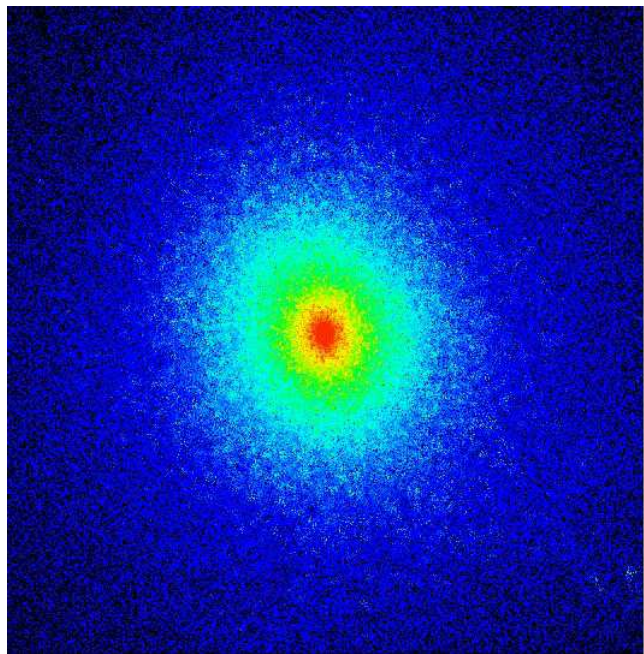


Figure 13. Density map of the smoothed mass distribution after randomizing the positions of the particles within the substructure haloes.

baryons is to steepen the mass profile to nearly isothermal with $\rho(r) \propto r^{-2}$ from a shallower r^{-1} cusp.

As already predicted by several (semi)analytic studies, our simulations show that this central concentration of baryons enables subhaloes to better withstand the tidal forces generated by the main halo. This leads to an increase in the total number of subhaloes, especially within the inner third of the virial radius, such that they follow the overall

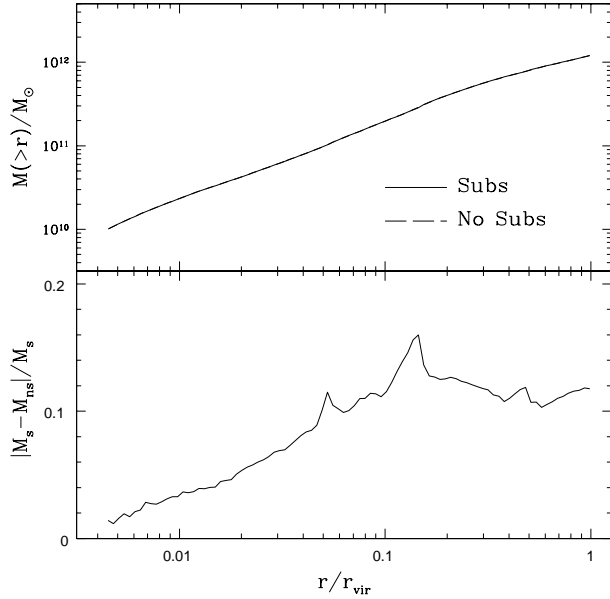


Figure 14. Mass versus radius before and after the removal of substructures, the overlap between the two curves is very good, in the lower panel the residuals are shown

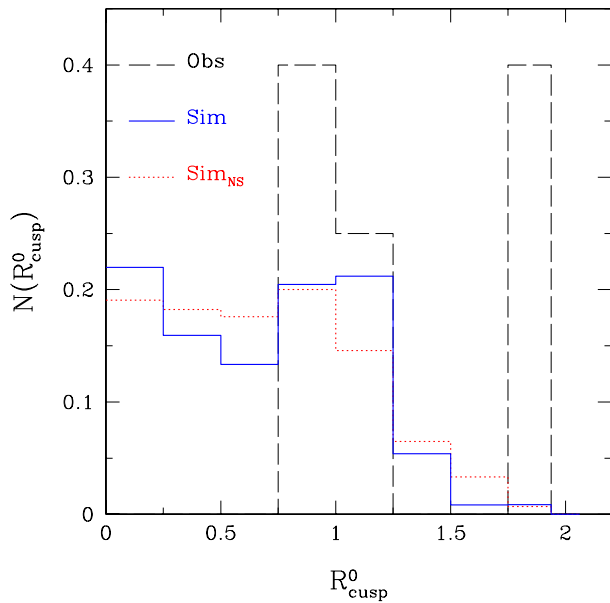


Figure 15. Distribution of R_{cusp}^0 values. The solid and dotted lines show the simulation results before and after the substructure removal. The long dashed line represents the observational data.

mass distribution. This is in excellent agreement with the distribution of galaxies within galaxy clusters. However on the scale of Galactic mass haloes, this increases the discrepancy between the numbers of surviving satellites in CDM models and the flat luminosity function observed within the Local Group. A possible solution to this problem may come from the early reionization of the universe from early struc-

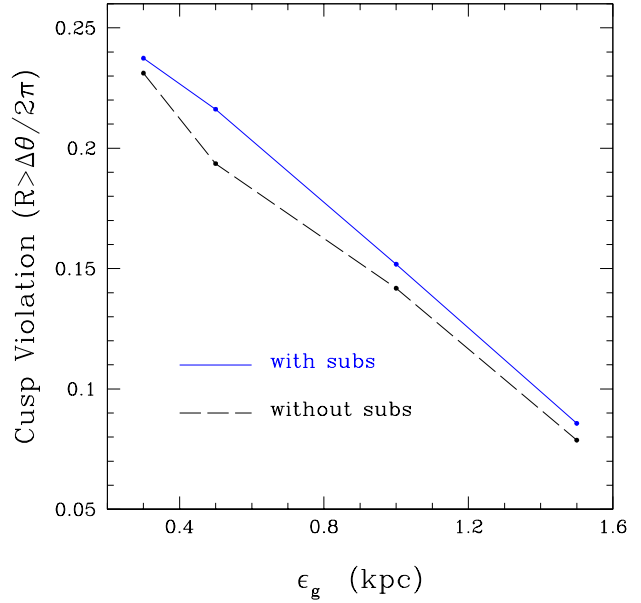


Figure 16. Fraction of total number of sources that violate the cusp relation as a function of the Gaussian smoothing length ϵ_g . Solid line is for the whole galaxy, dashed line for the galaxy *without* substructures (see text for its definition).

ture formation (Madau & Rees 2001). Reionization raises the entropy of the gas that is required to fuel galaxy formation, preventing it from accreting into small dark matter haloes and lengthening the cooling time of that gas which is accreted (Bullock et al 2001, Somerville et al 2002, Ricotti, Gnedin & Shull 2002). Moreover as suggested by Benson & Madau (2003) winds from pre-galactic starbursts and miniquasars may pollute the intergalactic medium (IGM) with metals and raise its temperature to a much higher level than expected from photoionization and so inhibit the formation of early galaxies.

A detailed study of the impact of reionization on the formation of dwarf galaxies in hydrodynamic simulation will be presented in a forthcoming paper (Macciò et al 2005b), where we show that with an appropriate choice of the reionization parameters and modeling it is possible to reconcile observational data with the steep mass function of haloes and subhaloes within the cold dark matter model.

In the second part of this work we have explored the consequences of the increased numbers of satellites for multiply lensed quasar images by foreground galactic mass haloes. In particular, the signatures on the violation of the so called cusp relation. Previous work have reached different conclusions on this issue: Bradac et al (2004), found an agreement between simulations and observations but their results were limited by the low resolution of their simulations. Amara et al (2004) (see also Mao et al 2004) have shown that is hard to reconcile the observed high number of cusp relation violation with results from simulations moreover they have also show that Shot noise due to the discreteness of the simulation (where every particle is in principle a substructure) plays an important role in changing the properties of the lens map. In order to disentangle the effect of substructures from the effect of having an intrinsic discrete distribu-

tion of matter we compared results between haloes with and without any substructure present. We have developed a new technique to remove the satellites from the simulation without changing the overall matter distribution of the primary lens. This analysis demonstrates that the impact on lensing of subhaloes in the mass range $10^7 - 10^{10} M_{\odot}$ is very small. Also having a number of subhaloes which is about 8 times higher of the observed one in this mass range, the number of multiple lensed QSO that show a violation of the cusp relation (defined as eq. 9) is less than 24%, in contrast with an observed one of about 60%. Our results extend down to subhaloes masses of $10^7 M_{\odot}$ due to the resolution limit of our simulations. Even considering the impact of smaller masses for subhaloes using an analytic approach does not help in solving the cusp relation problem (Macciò & Miranda 2005). A possible explanation could be that more variables must be taken into account in the lensing analysis, such as all the (sub)haloes that lie along the line of sight between us and the lens (see Chen et al. 2003, Metcalf 2004).

ACKNOWLEDGMENTS

The authors acknowledge J. Wadsley for development of the GASOLINE code and thank him for its use in this work and thank A. Kravtsov, D. Nagai, C. Mastroiello, L. Mayer, M. Miranda and P. Saha for useful discussions during the preparation of this work. We also thank the referee Hongsheng Zhao for his comments. AM also thanks S. Kazantzidis for the use of the *extract* software. JD is supported by the Swiss National Science Foundation. All the numerical simulations were performed on the zBox supercomputer (<http://www-theorie.physik.unizh.ch/~stadel/>) at the University of Zürich.

REFERENCES

- Amara, A., Metcalf, R.B., Cox, T.J. & Ostriker, J.P., 2004, *astro-ph/0411587*
- Blandford R., Narayan R., 1986, *ApJ*, 310, 568
- Bertschinger E., 2001, *ApJSS*, 137, 1
- Benson A. J., Madau P., 2003, *MNRAS*, 344, 835
- Blumenthal G. R., Faber S. M., Flores R., Primack J. R., 1986, *ApJ*, 301, 27
- Bradač M., Schneider P., Lombardi M., Steinmetz M., Koopmans L. V. E., Navarro J. F., 2004, *A&A*, 423, 797
- Bullock J. S., Kravtsov A. V., Weinberg D. H., 2000, *ApJ*, 539, 517
- Chen J., Kravtsov A. V., Keeton C. R., 2003, *ApJ*, 592, 24
- Chiba, M. 2002, *ApJ*, 565, 17
- Colin P., Klypin A. A., Kravtsov A. V., 2000, *ApJ*, 539, 561
- Dalal, N. & Kochanek, C. S. 2002, *ApJ*, 572, 25
- De Lucia G., Kauffmann G., Springel V., White S. D. M., Lanzoni B., Stoehr F., Tormen G., Yoshida N., 2004, *MNRAS*, 348, 333
- Diemand J., Moore B., Stadel J., 2004, *MNRAS*, 353, 624
- Diemand J., Moore B., Stadel J., 2004, *MNRAS*, 352, 535
- Gao L., White S. D. M., Jenkins A., Stoehr F., Springel V., 2004b, *MNRAS*, 355, 819
- Gao L., De Lucia G., White S. D. M., Jenkins A., 2004a, *MNRAS*, 352, L1
- Ghigna S., Moore B., Governato F., Lake G., Quinn T., Stadel J., 1998, *MNRAS*, 300, 146
- Ghigna S., Moore B., Governato F., Lake G., Quinn T., Stadel J., 2000, *ApJ*, 544, 616
- Gnedin O. Y., Kravtsov A. V., Klypin A. A., Nagai D., 2004, *ApJ*, 616, 16
- Governato, F., et al. 2004, *ApJ*, 607, 688
- Haardt F., Madau P., 1996, *ApJ*, 461, 20
- Hayashi E., et al., 2004, *MNRAS*, 355, 794
- Jackson, N., Nair, S., Browne, I. W. A., Wilkinson, P. N., Muxlow, T. W. B., de Bruyn, A. G., Koopmans, L., Bremer, M., et al., 1998, *MNRAS*, 296, 483
- Katz, N. 1992, *ApJ*, 391, 502
- Katz N., White S. D. M., 1993, *ApJ*, 412, 455
- Keeton, C. R., Gaudi, B. S., & Petters, A. O. 2003, *ApJ*, 598, 138
- Keeton, C. 2002, preprint, *astro-ph/0112350*
- Keeton, C. R. 2003, *ApJ*, 584, 664
- Klypin A., Kravtsov A. V., Valenzuela O., Prada F., 1999, *ApJ*, 522, 82
- Kochanek, C. S. & Dalal, N. 2004, *ApJ*, 610, 69
- Koopmans, L. V. E., Biggs, A., Blandford, R. D., Browne, I. W. A., Jackson, N. J., Mao, S., Wilkinson, P. N., de Bruyn, A. G., et al., 2003, *ApJ*, 595, 712
- Kravtsov A. V., Klypin A. A., Khokhlov A. M., 1997, *ApJS*, 111, 73
- Kravtsov A. V., Gnedin O. Y., Klypin A. A., 2004, *ApJ*, 609, 482
- Loeb A., Peebles P. J. E., 2003, *ApJ*, 589, 29
- Macciò A. V., 2005, *MNRAS*, 361, 1250
- Macciò A. V. & Miranda M., 2005, preprint *astro-ph/0509598*
- Madau P. & Rees M. J., 2001, *ApJ*, 551, L27
- Mao S., 1992, *ApJ*, 389, 63
- Mao S., Schneider P., 1998, *MNRAS*, 295, 587
- Mao S., Jing Y., Ostriker J. P., Weller J., 2004, *ApJ*, 604, L5
- Mateo M. L., 1998, *ARA&A*, 36, 435
- Metcalf, R. B. 2002, *ApJ*, 580, 696
- Metcalf, R. B. & Madau, P. 2001, *ApJ*, 563, 9
- Metcalf, R. B. & Zhao, H. 2002, *ApJL*, 567, L5
- Metcalf, R. B. 2004, preprint *astro-ph/0412538*
- Moore B., Katz N., Lake G., 1996, *ApJ*, 457, 455
- Moore B., Governato F., Quinn T., Stadel J., Lake G., 1998, *ApJ*, 499, L5
- Moore B., Ghigna S., Governato F., Lake G., Quinn T., Stadel J., Tozzi P., 1999, *ApJ*, 524, L19
- Moore, B. 2001, *AIP Conf. Proc.* 586: 20th Texas Symposium on relativistic astrophysics, 586, 73
- Nagai D., Kravtsov A. V., 2005, *ApJ*, 618, 557
- Navarro J. F., Frenk C. S., White S. D. M., 1996, *ApJ*, 462, 563
- Patnaik, A. R. & Narasimha, D. 2001, *MNRAS*, 326, 1403
- Reed D., Governato F., Quinn T., Gardner J., Stadel J., Lake G., 2005, *MNRAS*, 380
- Ricotti M., Gnedin N. Y., Shull J. M., 2002, *ApJ*, 575, 49
- Schneider, P. & Weiss, A. 1992, *A&A*, 260, 1
- Sluse, D., Surdej, J., Claeskens, J.-F., Hutsemékers, D., Jean, C., Courbin, F., Nakos, T., Billeres, M., et al., 2003, *A&A*, 406, L43
- Somerville R. S., 2002, *ApJ*, 572, L23
- Stadel J., 2001, PhD thesis, U. Washington
- Wadsley, J. W., Stadel, J., & Quinn, T. 2004, *New Astronomy*, 9, 137
- Zakharov, A. F. 1995, *A&A*, 293, 1
- Zentner A. R., Bullock J. S., 2003, *ApJ*, 598, 49
- Zentner, A. R., Kravtsov, A. V., Gnedin, O. Y., & Klypin, A. A. 2005a, *ApJ*, 629, 219
- Zentner, A. R., Berlind, A. A., Bullock, J. S., Kravtsov, A. V., & Wechsler, R. H. 2005b, *ApJ*, 624, 505